# Hollow ZnO microspheres self-assembled from rod-like nanostructures: morphology-dependent linear and Kerr-type nonlinear optical properties

Azadeh Haghighatzadeh[1,*], Babak Mazinani[2], Masood Ostad[1,3], Mohammadreza Shokouhimehr[4], and Joydeep Dutta[5,*] (ID)

[1] *Advanced Surface Engineering and Nano Materials Research Center, Department of Physics, Ahvaz Branch, Islamic Azad University, Ahvaz, Iran*

[2] *Department of Materials Engineering, Malayer University, Malayer, Iran*

[3] *Department of Physics, Khouzestan Science and Research Branch, Islamic Azad University, Ahvaz, Iran*

[4] *Department of Materials Science and Engineering, Research Institute of Advanced Materials, Seoul National University, Seoul 08826, Republic of Korea*

[5] *Functional Materials, Applied Physics Department, KTH Royal Institute of Technology, Hannes Alfvéns väg 12, 114 19 Stockholm, Sweden*

## ABSTRACT

Hollow nanostructures have attracted attention because of their unique physio-chemical properties and broad potential applications in electronics, optics and photonics. In this study, a facile hydrothermal approach was developed to fabricate hollow ZnO microspheres via self-assembled rod-like nanostructures. The morphology-controlled synthesis was conducted by altering hydrothermal treatment temperature (150, 200 and 250 °C) in solutions containing zinc acetate dihydrate precursor and glycerol as the stabilizing agent. The morphological observations indicated that hydrothermally grown ZnO architectures could be reasonably adjusted by modulating hydrothermal reaction temperature. Possible growth routes are proposed to elucidate the formation process of ZnO microspheres with the rod-like nanostructures. Morphology-dependent absorbance and emission along with red-shifts with improved crystalline qualities were observed with increasing hydrothermal growth temperature. Kerr-type nonlinear optical characteristics examined using single-beam Z-scan technique in the near infrared spectral range under nanosecond Nd-YVO$_4$ laser pulses showed positive values of nonlinear refraction providing an evidence of self-focusing behaviors at the excitation wavelength of 1064 nm in all the samples studied. The highest Kerr-type nonlinear susceptibility was estimated to be $2.31 \times 10^{-6}$ esu for hollow ZnO microspheres grown at 250 °C, suggesting synergistic effects of surface morphologies on optical nonlinearities.

Address correspondence to E-mail: azadeh.haghighatzadeh.physics@gmail.com; a.haghighatzadeh@iauahvaz.ac.ir; joydeep@kth.se

Springer

# 1 Introduction

Kerr-type nonlinear optics (bound-electronic nonlinear refraction) has been an intensive area of research since the observation of birefringence in 1875 by Scottish physicist John Kerr [1]. Exotic optical phenomenon, e.g., self-phase modulation for the generation of optical solitons, and self-lensing of laser beams, offers application opportunities for quantum non-demolition measurements, quantum-bit regeneration, quantum-state teleportation, optical solitons, all-optical switching, etc., which are commonly realized through optical Kerr effects [2, 3]. The improved Kerr nonlinearities along with reduced linear and nonlinear absorption characteristics provide new possibilities to control nonlinear interactions of optical systems for low light powers showing high sensitivities [4–8]. Such notable achievements have been the inspiration for the development of optical materials garnering the advantages of enhanced Kerr nonlinearities. With the progress in manufacturing technologies, a variety of materials including semiconductors [9, 10], polymers [11], organic liquids [1], plasmonic materials [12], and YAG crystals [3] have been explored showing considerable Kerr nonlinearities. Thakur et al. analyzed the fast, tunable and broadband optical Kerr nonlinearity of graphene in the near-infrared spectral region [11]. Qian et al. presented giant Kerr response of ultrathin gold films showing quantum size effects [12]. Li et al. demonstrated picosecond Z-scan study of bound electronic Kerr effect in $LiNbO_3$ crystal associated with two-photon absorption [13]. In another interesting study, Wang and colleagues measured enhanced Kerr nonlinearity via atomic coherence in a three-level atomic system [14]. According to previously published research articles, the optical bi-stability/multi-stability and its plausible applications in all-optical switching nanodevices can be realized through Kerr nonlinearities by changing the optical anisotropy and geometric parameters [15, 16].

Nano-sized metal-oxide semiconductors with desirable optical functions such as large nonlinearities and short response time have drawn significant attention for the realization of new-generation nonlinear photonic devices in the past few decades [17].

Several research studies have attempted to provide cohesive understanding of the third-order nonlinearity, in particular, the Kerr type nonlinearity in metal-oxide-related semiconducting materials. For instance, Yan and co-workers performed a systematic study of ultrafast nonlinear optical properties and optical Kerr effect in doped zinc oxide (ZnO) nanowires at 800 nm [10]. Merikhi et al. examined magneto-optical Kerr effect in $ZnTMO_2$ chalcopyrite, where TM was chromium (Cr), manganese (Mn), iron (Fe), cobalt (Co) and nickel (Ni) by considering that polar Kerr angles range from the infrared (IR) to ultraviolet (UV) radiation [18]. In an earlier work, we have reported enhanced Kerr-type third-order optical susceptibility for silver/cerium oxide ($Ag/CeO_2$) Schottky-type nanostructures with near infrared irradiation [19, 20].

Zinc Oxide (ZnO) is a II–VI group n-type compound semiconductor that has long been of interest for a variety of applications ranging from blue and ultraviolet optical devices to chemical sensors as it possesses unique features such as wide optical bandgap, high linear refractive index, large excitonic binding energy, high electron mobility nature, low electrical resistance, and high chemical activity, amongst others [21–25]. Since the report of ZnO thin films in 1960, various physical and chemical synthesis routes have been developed and applied to gas sensors, transducers, solar cells, photocatalysis, and photonic instruments [26]. Compared to other semiconductor materials, ZnO enjoys the advantage of being relatively facile to form into complicated geometrical morphologies using solution synthesis techniques due to the polar nature of hexagonal wurtzitic lattice [26]. Morphology-controlled synthesis by various approaches including chemical vapor deposition [27, 28], hydrothermal solution synthesis [29–31] and sol–gel processing [32] leads to a wide range of distinct ZnO nanostructures such as rods [33, 34], pyramids [35, 36], stars [37], flowers [38], etc. There are many published work describing the fabrication and performance of ZnO-based nanorods or nanowires due to low dimensionalities leading to quantum confinement effects [26]. For example, Baruah et al. studied the effect of pH variation on the dimension and morphology of ZnO nanorods grown through hydrothermal process on pre-seeded glass

substrates at temperature $\sim 100\,°C$ [39]. The synthesis of three-dimensional nanostructures consisting of a mass of organized one-dimensional or two-dimensional building blocks have shown enhanced optoelectronic properties due to the functioning as both the building blocks as well as the interconnections [40–45]. Several investigations have demonstrated hollow ZnO microspheres assembled by one-dimensional building units exhibiting unique properties such as low densities, enlarged surface areas, and shortened transport distances presenting highly efficient surface permeability [46]. Many scientists consider that ZnO semiconductor nanostructures with improved nonlinearities (e.g., large value of the third-order optical susceptibility) can be utilized as potential materials for the assembly of instruments based on nonlinear optics [47–49]. Consequently, numerous studies have attempted to explore nonlinear optical characteristics in ZnO-based micro/nanostructures. For example, Loiko et al. has shown that ZnO nanorods grown on various optical surfaces are promising broadband saturable absorbers for nanosecond near-IR lasers in bulk and waveguide geometries [50]. Second and third harmonic generation measurements in amorphous ZnO thin films has been performed by rotational Maker fringe technique using Nd:YAG laser at 1064 nm in picosecond range for the verification of the nonlinear optical properties [51]. In addition, it has been found that the restricted motion of excitons and phonons can impact nonlinear functionalities of the nanomaterials depending on their shapes and sizes [52–54]. Indeed, many research articles have illustrated diverse methodologies to understand the morphology-dependent optical nonlinearities. For example, Maki et al. described morphology-related third-order nonlinear optical responses of polydiacetylene nanofibers owing to the long effective π-conjugation lengths [55]. In another study, Oikawa reported hybridized organic nanocrystals as optically functional materials with enhanced optical nonlinearities depending upon crystal size and shape due to the quantum confinement effects [56].

In a study by Li et al., a series of mesoporous hollow ZnO microspheres were synthesized via a hydrothermal method to investigate the influence of reagent ratio on morphologies and gas sensing properties [57]. It is believed that in addition to the experimental parameters, e.g., the metal precursor concentration and stabilizing agents, the morphology can be influenced by reaction conditions such as growth temperature and time [58]. Therefore, it is desirable to exploit the role of different synthetic conditions for modifying the morphological characteristics of ZnO nanostructures and the subsequent optical nonlinearities upon exposure to high-intensity light beams. In this study we have developed morphological characteristics of ZnO microspheres synthesized by modifying a procedure introduced Li et al. [57] and evaluated the linear and nonlinear optical properties of the three-dimensional ZnO nanostructures. Three important issues are focused in the current research: (*i*) effect of different hydrothermal temperatures (150, 200, and 250 °C) on morphological characteristics, (*ii*) investigating morphology dependent spectral optics and (*iii*) examining Kerr-type nonlinear parameters using single-beam Z-scan technique. To the best of our knowledge, this is the first report on the optical nonlinearities of such three-dimensional ZnO microstructures in the near infra-red region (1064 nm). In general, the synthesized hollow ZnO microstructures can offer several advantages originating from their unique properties, e.g., low density, high surface area, and shortened transport distances, providing efficient surface permeability [46], which can improve practical applications in photonic devices.

## 2 Experimental procedures

Zinc acetate dihydrate [$C_4H_6O_4Zn·2H_2O$, molecular weight: 219.49 g/mol, 98%], Glycerol [$C_3H_8O_3$, molecular weight: 92.09 g/mol, 85%], and absolute Ethanol [$C_2H_6O$, molecular weight: 46.07 g/mol, 96%] were purchased from Merck and employed as received without further purifications. Both distilled and deionized water were used in all experiments.

ZnO samples were synthesized by modifying a previously reported method via a hydrothermal treatment route using zinc acetate dihydrate precursor and glycerol as stabilizing agent [57]. Figure 1 schematically describes the overall synthetic procedure for the synthesis of ZnO microspheres. During a typical synthesis, 1 g of zinc acetate dihydrate was dissolved in 10 mL of deionized water under vigorous stirring for 30 min and followed by the addition of 75 mL of glycerol. The reaction solution was mixed for 1 h in a magnetic stirring bath and then transferred into a 150 mL Teflon lined autoclave, where it

**Fig. 1** Schematic representation of the synthetic procedure for the preparation of ZnO microspheres

was maintained at different temperatures of 150, 200, and 250 °C for 24 h. After gradual cooling to the room temperature, the resultant precipitate was filtered and washed with distilled water and ethanol several times to remove any residual ions. The wet product was dried at 60 °C for 24 h and calcined at 400 °C for 4 h. The resultant ZnO samples were then labeled as S150, S200, and S250 depending on the applied hydrothermal growth temperatures of 150, 200 and 250 °C, respectively.

UV–Vis diffuse reflectance spectra (DRS) were measured in Avaspec-2048-TEC spectrophotometer. Photoluminescence (PL) spectra were obtained using a Perkin Elmer LS55 fluorescence spectrophotometer equipped with xenon lamp to detect emission characteristics under an excitation wavelength fixed at 250 nm. Nonlinear characteristics of third-order optics were examined using standard single-beam Z-scan technique according to the experimental optical setup reported in a previously published study [59]. ZnO samples (0.01 g of powder dispersed in 20 mL of ethanol) were poured in a 1 mm thickness quartz cell, and irradiated using a pulsed Nd-YVO$_4$ laser system emitting 1064 nm wavelength with a radiance power of 20 mW, pulse duration of 50 ns, repetition rate of 10 kHz. The beam intensity was determined to be $3.98 \times 10^6$ W/m$^2$ for beam waist of $\omega_0 = 32$ μm and the diffraction length $z_0 = 3$ mm at the foci of a 300 mm focal length lens. The samples were mounted along the optical axis in a motorized transition stage with 0.65 mm steps. The morphology and microstructure of the samples were

investigated in a field emission scanning electron microscope (FESEM, Zeiss SIGMA VP-500) and a transmission electron microscope (TEM, Philips-CM120-120 kV). All the micrographs were analyzed using ImageJ software for estimating average particle sizes from 50 to 70 particles in each micrograph. Phase characterizations and surface functional group identification are provided in the supporting information.

## 3 Results

### 3.1 Linear characterization

Room-temperature steady-state photoluminescence (PL) patterns of ZnO samples obtained at different hydrothermal temperatures were measured in wavelength ranging from 270 to 800 nm with an excitation wavelength of 250 nm (4.96 eV) as shown in Fig. 2. It can be observed that ZnO samples prepared at 150 °C show a strong short-wavelength (SW) emission band around ~ 398 nm (3.11 eV) along with a weaker long-wavelength (LW) band centered at 670 nm (1.85 eV). The SW band ranges from 300 to 550 nm with full width at half maximum (FWHM) of ~ 126 nm, while the LW band covers visible region from 590 to 800 nm with a FWHM of about ~ 187 nm. The extended emission pattern of SW band is from a combination of near band-gap emissions (NBEs) originating from transitions related to band-edge free excitons and those bound to the
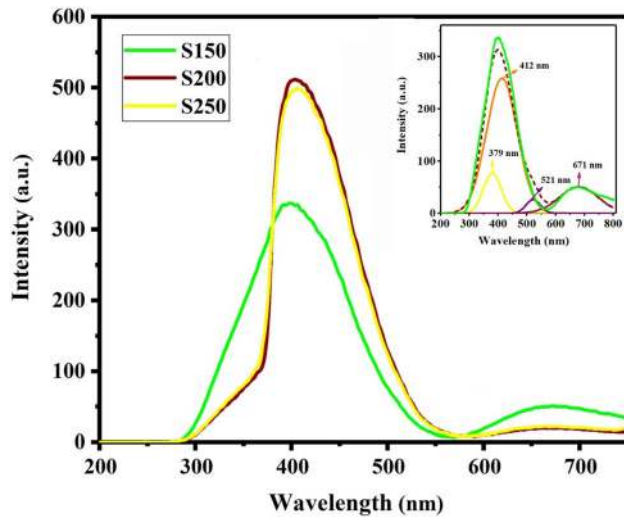
**Fig. 2** PL emission patterns of ZnO samples prepared at different hydrothermal temperatures. The inset shows PL spectrum of ZnO sample treated at a temperature of 150 °C

shallow states. However, the LW emission band peaking at the visible wavelength of ∼ 670 nm can be attributed to the deep level emissions. The shallow and deep states formed in ZnO forbidden gap generally originate from four main point defects in the ZnO lattices including (i) zinc vacancy ($V_{Zn}$), (ii) zinc interstitials ($Zn_i$), (iii) oxygen vacancy ($V_O^{\bullet*}$), and (iv) oxygen interstitials ($O_i$) [60]. These defect configurations arise from zinc–oxygen nonstoichiometry, abundance of which is dependent on preparation conditions [61]. The spectral pattern of sample S150 was fitted with a multi-peak Gaussian function to distinguish the different emission peaks. The results are presented in the inset of Fig. 2; the SW band can be deconvoluted into three Gaussian peaks centered at 379, 412 and 521 nm, respectively, in which the UV emission band at 379 nm can be ascribed to the NBEs owing to the free exciton-exciton recombination in ZnO lattice [62]. In addition, $Zn_i$ and $V_O^{\cdot*}$ with transitions to ZnO valence band are considered to be responsible for 412 nm violet emission and 521 nm green emissions [62]. The red emission peak ∼ 670 nm is normally associated with deep level oxygen interstitials [61].

It can be seen in Fig. 2 that increase of hydrothermal growth temperature causes an increase in the excitonic PL intensity with a subsequent reduction of the FWHM of the SW-dependent bands (Table 1). Indeed, the SW bands with more intense and sharper peaks in spectral patterns of samples S200 and S250

suggest higher-quality emissions, which can be attributed to the improvement in the crystal structure of ZnO. The increased SW band emission intensity reveals enhanced excitonic transitions in samples prepared at higher temperatures. A decrease in deep level emission-related intensities is detected in samples synthesized at higher temperatures. It should be noted that it is plausible to evaluate the concentration of intrinsic defects by calculating the PL intensity ratio of the LW bands to that of the SW bands [63, 64]. Accordingly, the dimensionless parameter $I_{LW}/I_{SW}$ could be defined and the calculated data are listed in Table 1. The obtained results demonstrate the possibility of localizing more number of deep trap states in S250 sample compared to the samples synthesized at lower hydrothermal temperatures. It can be also concluded from Fig. 2 that the increase in hydrothermal growth temperature leads to red shifts of the SW emission band. The SW emission band edges of samples S200 and S250 show red shifts of ∼ 4 and ∼ 5 nm compared to the sample S150. NBE-related energies can be estimated from the SW emission band's based on $E_{NBE}(eV) = 1240/\lambda_{SW}(nm)$ [49], where $E_{NBE}$ and $\lambda_{SW}$ stand for NBE-related energy and the wavelength of emission peak relevant to the SW band, respectively. Table 1 tabulates numerical results obtained from the SW emission band analysis. As given in Table 1, the NBE-related energies are found to be at 3.11, 3.08, and 3.07 eV for samples S150, S200 and S250, respectively. The NBE-related energies were further confirmed by UV–Vis analysis and quantified by Tauc Plots (Figs. 3 and 4).

Light absorbance of ZnO samples prepared at different hydrothermal temperatures was recorded in a wavelength range of 300–600 nm, and results are shown in Fig. 3. It is obvious from Fig. 3 that the increase of hydrothermal growth temperature leads to reduced light absorption in both UV and Visible wavelength ranges. This result verifies that higher hydrothermal synthesis temperature leads to an improvement of the crystalline quality of ZnO. All the as-synthesized ZnO samples showed significant optical absorption peak at ∼ 371 nm due to the intrinsic band-gap adsorption of ZnO crystals shifting towards visible region.
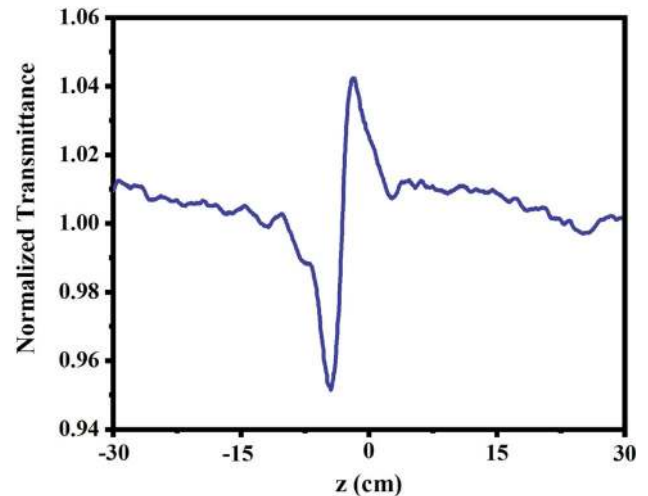
### 3.2 Nonlinear optical characterization

The dependence of optical refractive index ($n$) and absorption coefficient ($\alpha$) on the laser intensity ($I$) in a

**Table 1** Linear optical parameters of ZnO samples treated at different hydrothermal temperatures

| Sample | FWHM$_{SW}$ (nm) | $\lambda_{SW}$ (nm) | ENBE (eV) | $\lambda_{LW}$ (nm) | E$_{LW}$ (eV) | I$_{LW}$/I$_{SW}$ |
|---|---|---|---|---|---|---|
| S150 | 126 | 398 | 3.11 | 670 | 1.85 | 0.15 |
| S200 | 93 | 402 | 3.08 | 670 | 1.85 | 0.03 |
| S250 | 93 | 403 | 3.07 | 670 | 1.85 | 0.04 |
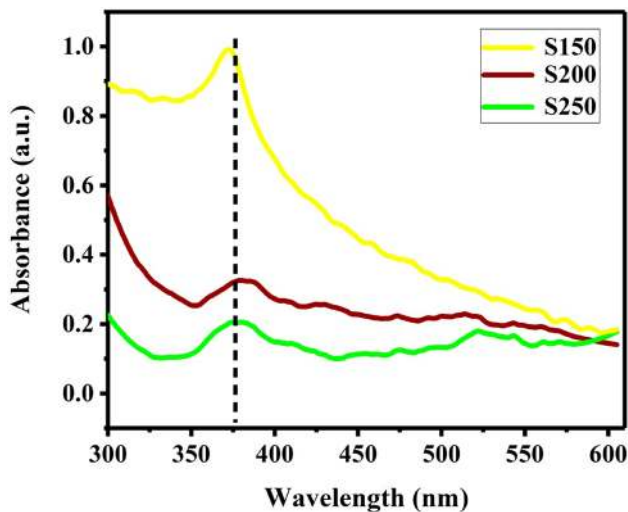


**Fig. 3** UV–Vis absorbance spectra of ZnO samples treated at different hydrothermal temperatures



**Fig. 4** Normalized Z-scan curves of ethanol

regime related to the Kerr-type nonlinear response can be expressed as $n = n_0 + n_2 I$ and $\alpha = \alpha_0 + \beta I$ [12, 65], where, $n_0$ and $\alpha_0$ are the linear refractive index and the linear absorption coefficient, respectively. $n_2$ and $\beta$ denote the nonlinear refractive index and the nonlinear absorption coefficient, respectively. In a system showing a negligible linear absorption, the electronic Kerr nonlinearity is connected with understanding the third-order term of polarization ($P$) induced in a medium by radiant light beams in a series of increasing powers of the electric field ($E$) as $P = \varepsilon_0(\chi^{(1)}E + \chi^{(2)}E^2 + \chi^{(3)}E^3 + ...)$ [66]. Here, $\chi^{(1)}$ denotes a linear susceptibility of the medium and $\chi^{(2)}$ and $\chi^{(3)}$ are the second- and third-order nonlinear susceptibility tensors, respectively. The real and imaginary parts of the third-order nonlinear optical susceptibility are generally proportional to the nonlinear refractive index ($n_2$) and the nonlinear absorption coefficient ($\beta$) given as $\text{Re}(\chi^{(3)}) = \frac{4\varepsilon_0 c n_0^2 n_2}{3}$ and $\text{Im}(\chi^{(3)}) = \frac{\varepsilon_0 c n_0^2 \lambda \beta}{3\pi}$ [67], where, $\lambda$, $c$ and $\varepsilon_0$ are the excitation wavelength, the velocity of light, and the electric permittivity of free space, respectively. As reported in Ref. [66], the linear refractive index can be determined with help of Lorentz-Lorentz relation

based on $1 - \frac{n_0^2 - 1}{n_0^2 + 1} = \left(\frac{E_g}{20}\right)^{1/2}$ equation, where $E_g$ is optical band-gap. Corresponding to the above results, the third-order susceptibility can be calculated as $|\chi^{(3)}| = \sqrt{\text{Re}(\chi^{(3)}) + \text{Im}(\chi^{(3)})}$ [49]. Here, $\chi^{(3)}(SI) = 4\pi \times (10^{-8}/9)\chi^{(3)}(esu)$ conversion relation can be utilized to convert the unit from (SI) to (esu) [49].

The characterization of the third-order nonlinear refraction for hydrothermally grown ZnO samples were carried out by dividing closed-aperture (CA) Z-scan data by the open-aperture (OA) traces to eliminate the possible effects emanating from the nonlinear absorption features. Ethanol was used for the Z-scan examinations as a solvent, which could potentially show nonlinear responses to incident laser beams. Therefore, nonlinear effect of the solvent was first determined under identical experimental conditions and then subtracted from Z-scan data recorded from each measured samples (Fig. 4). The nonlinear contribution of the solvent turns out to be positive, as documented by a valley preceding a peak in the transition curve.

The normalized divided Z-scans of ZnO samples obtained at different hydrothermal temperatures after elimination of the nonlinear effects of the solvent are shown in Fig. 5. The normalized divided Z-

scans for all the tested samples indicate a minimum followed by a maximum in the normalized transmittance. The valley-to-peak configurations around the focal point suggest self-focusing behaviors due to positive lens effects. Numerical information of nonlinear refraction characteristics ($n_2$) were obtained from the differences between the valley and the peak ($\Delta T_{PV} = T_P - T_V$), where valley-to-peak shapes the curves in which $T_P$ and $T_V$, denoted as the normalized peak and valley transmittances, respectively. In addition, the difference between the peak and valley transmittances ($\Delta T_{PV}$) in the absence of nonlinear absorption can be written in terms of the third-order nonlinear refraction ($n_2$) as $\Delta T_{PV} = 0.406(1 - S)^{0.27}\left(2\pi/\lambda\right)n_2 I_0 L_{eff}$ [68], where $S = 0.34$ is the aperture transmittance, $\lambda$ is the irradiated beam wavelength and $I_0$ is the laser beam intensity at the focus. $L_{eff}$ is the effective length of sample which can be determined by using $L_{eff} = \frac{1 - \exp(-\alpha_0 L)}{\alpha_0}$ equation [69]. $L$ stands for the sample thickness while $\alpha_0$ is the linear absorption coefficient. The linear absorption characteristics of ZnO samples dispersed in ethanol were investigated using near IR (NIR) absorbance spectra (Fig. 6). All the tested samples revealed a negligible linear absorption at 1064 nm. Linear absorption coefficients was estimated from the Beer and Lambert' law as $\alpha_0 = 2.303\,(A/t)$[70], where $A$ is absorbance, and $t = 1$ cm is the thickness of the samples. In Table 2, we have summarized the numerical results of linear absorption coefficients and the

corresponding effective lengths. The estimated effective lengths are approximately equal to the thickness of the cuvette (1 cm). Thus, it can be concluded from the theoretical nonlinear refractive indices that the larger differences in Z-scan transmittances would lead to higher nonlinear refractions in the materials with negligible linear absorption. The numerical values related to the third-order nonlinear refraction parameters for ZnO samples prepared at different hydrothermal growth temperatures are summarized in Table 2, exhibiting a changing trend as S250 > S200 > S150 for the estimated nonlinear refractions.

The suitability of hydrothermally grown ZnO samples as nonlinear absorbers when irradiated with a wavelength of 1064 nm was evaluated from the OA during Z-scan. Normalized OA Z-scan data for ZnO samples prepared at different hydrothermal temperatures are shown in Fig. 7. ZnO samples do not show considerable signal owing to nonlinear absorption behaviors. Subsequently, the third-order optical susceptibility defines itself only through the real part of the third-order susceptibility due to purely nonlinear refraction effects. It is important to note that the refractive part of the third-order susceptibility also known as Kerr-type nonlinearity impact nonlinear optics considerably [71]. Therefore, the third-order nonlinear optical susceptibility (Kerr-type susceptibility) exhibits a trend similar to that obtained for nonlinear refractive indices. The estimated values of the Kerr-type optical susceptibilities of ZnO samples
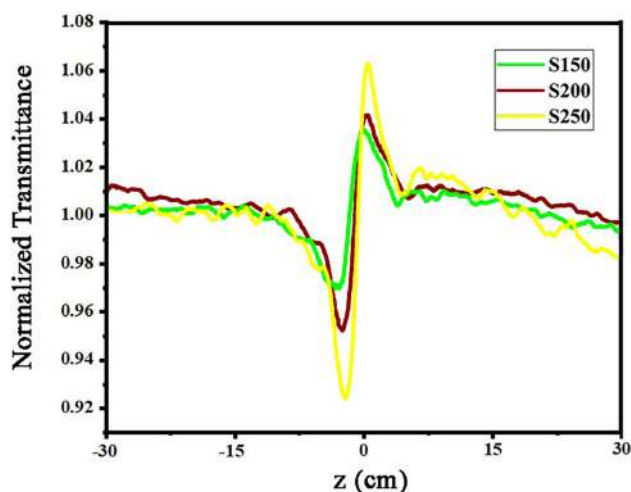


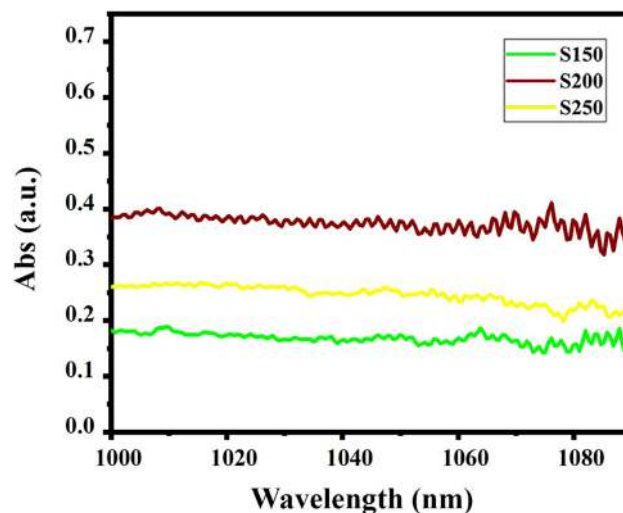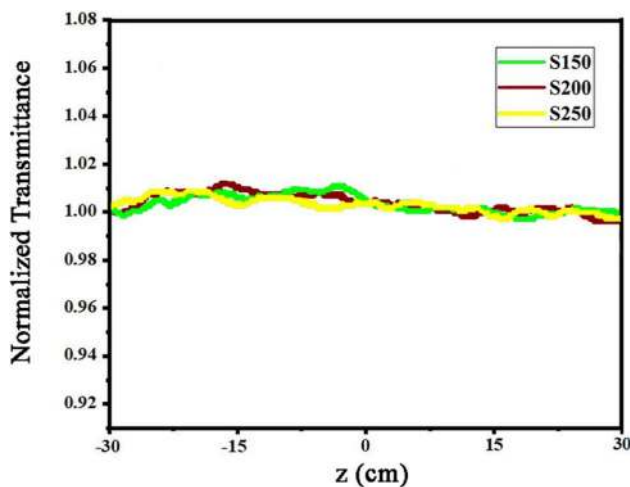**Fig. 5** Normalized Z-scan curves of ZnO samples treated at different hydrothermal temperatures



**Fig. 6** NIR absorption spectra of ZnO samples prepared at different hydrothermal temperatures

**Table 2** Results of the third-order nonlinear parameters of ZnO samples prepared at different hydrothermal temperatures (Wavelength 1064 nm, Pulse duration 50 ns, Repetition rate 10 kHz, Radiance power 20 mW, and Laser intensity $3.98 \times 10^6$ W/m$^2$)

| Sample | $T_P$ | $T_V$ | $\Delta R_{PV}$ | $\alpha$(cm$^{-1}$) | $L_{eff}$ (m) | $n_o$ | $n_2$ (W/m$^2$) | $X^{(3)}$ (esu) |
|--------|-------|-------|-----------------|---------------------|---------------|-------|-----------------|-----------------|
| S150 | 1.036 | 0.969 | 0.067 | 0.368 | $0.113 \times 10^{-2}$ | 2.29 | $0.78 \times 10^{-11}$ | $1.07 \times 10^{-5}$ |
| S200 | 1.042 | 0.951 | 0.091 | 0.829 | $0.096 \times 10^{-2}$ | 2.31 | $1.06 \times 10^{-11}$ | $1.42 \times 10^{-5}$ |
| S250 | 1.064 | 0.922 | 0.142 | 0.529 | $0.108 \times 10^{-2}$ | 2.34 | $1.66 \times 10^{-11}$ | $2.31 \times 10^{-5}$ |



**Fig. 7** Normalized OA Z-scan curves ZnO samples prepared at different hydrothermal temperatures

have been summarized in Table 2. Accordingly, the highest Kerr-type susceptibility ($2.31 \times 10^{-6}$ esu) was observed for the sample S250 exhibiting a value approximately 2.15 times larger than that of the lowest value ($1.07 \times 10^{-6}$ esu) obtained in sample S150.

### 3.3 Morphological characterization

The morphology and distribution of ZnO sample synthesized at a temperature of 150 °C were studied using FESEM and TEM analysis. FESEM micrographs of sample S150 at different magnifications are presented in Fig. 8a–c. The lower magnification FESEM images (Fig. 8a and b) present an aggregation of monodispersed ZnO particles. The magnified FESEM image shows (Fig. 8c) that sample S150 includes a uniform distribution of pseudo-sphere-like particles with particle sizes ranging from $\sim$ (25 nm $\pm$ 1 nm) to (35 nm $\pm$ 1 nm). The nanostructures of this sample were further clarified by TEM study (Fig. 8d), demonstrating the formation of sphere-like particles with a mean size of $\sim$ (34 nm $\pm$ 1 nm).

Figure 9 exhibits FESEM images from sample S200 at different magnifications. The overview image shown in Fig. 9a indicates the formation of sphere-like architectures in two distinguishable dimensional regions. Microstructures observed in Fig. 9a reveal spheres with diameters of (1–2 μm $\pm$ 1 μm) and (4–13 μm $\pm$ 1 μm) relevant to smaller and bigger dimensional regions, respectively. The average diameters were measured to be $\sim$ (1.4 μm $\pm$ 0.1 μm) and (9 μm $\pm$ 1 μm), for smaller and bigger microspheres, respectively. The high magnification FESEM image (Fig. 9b) clearly indicates that micro-scale sphere-like nanostructures form consisting of accumulated ZnO particles. Figure 9c shows that the large-scale ZnO microspheres are composed of polygonal particles with a size distribution between (70 nm $\pm$ 1 nm) to (350 nm $\pm$ 1 nm). Small-scale microspheres (Fig. 9d) are assembled in a bundle of rod-shaped nanostructures oriented parallel to the radius of sphere from end to end. The rod-shaped nanostructures exhibit a mean diameter and length of $\sim$ (110 nm $\pm$ 1 nm) and (330 nm $\pm$ 1 nm), respectively.

Figure 10 shows the FESEM images of the sample synthesized at 250 °C. The overview image illustrated in Fig. 10a reveals the formation of microspheres with an approximately more uniform size distribution compared to those obtained at 200 °C. Measurements performed based on FESEM images indicate an average size of $\sim$ (4 μm $\pm$ 1 μm) for the diameter of formed microspheres. The magnified image displayed in Fig. 10b also verifies the formation of monodispersed microrods with an average length of $\sim$ (1.0 μm $\pm$ 0.1 μm), and an average diameter of $\sim$ (130 nm $\pm$ 1 nm) in addition to micro-scaled spherical nanostructures in S250 samples. ZnO microspheres as shown in Fig. 10c are assembled by polygonal nanostructures, having a size distribution between $\sim$ (38 nm $\pm$ 1 nm) to (200 nm $\pm$ 1 nm). Comparing Figs. 9c and 10c, we can observe the formation of microstructures with porous exterior at 250 °C compared to those synthesized at 200 °C. In addition, an increase in hydrothermal treatment temperature has led to a decrease in the average diameter of ZnO nanorods obtained for S250 sample compared to those observed for S200 sample. As

**Fig. 8** **a**–**c** FESEM and **d** TEM images of ZnO sample prepared at hydrothermal temperature of 150 °C
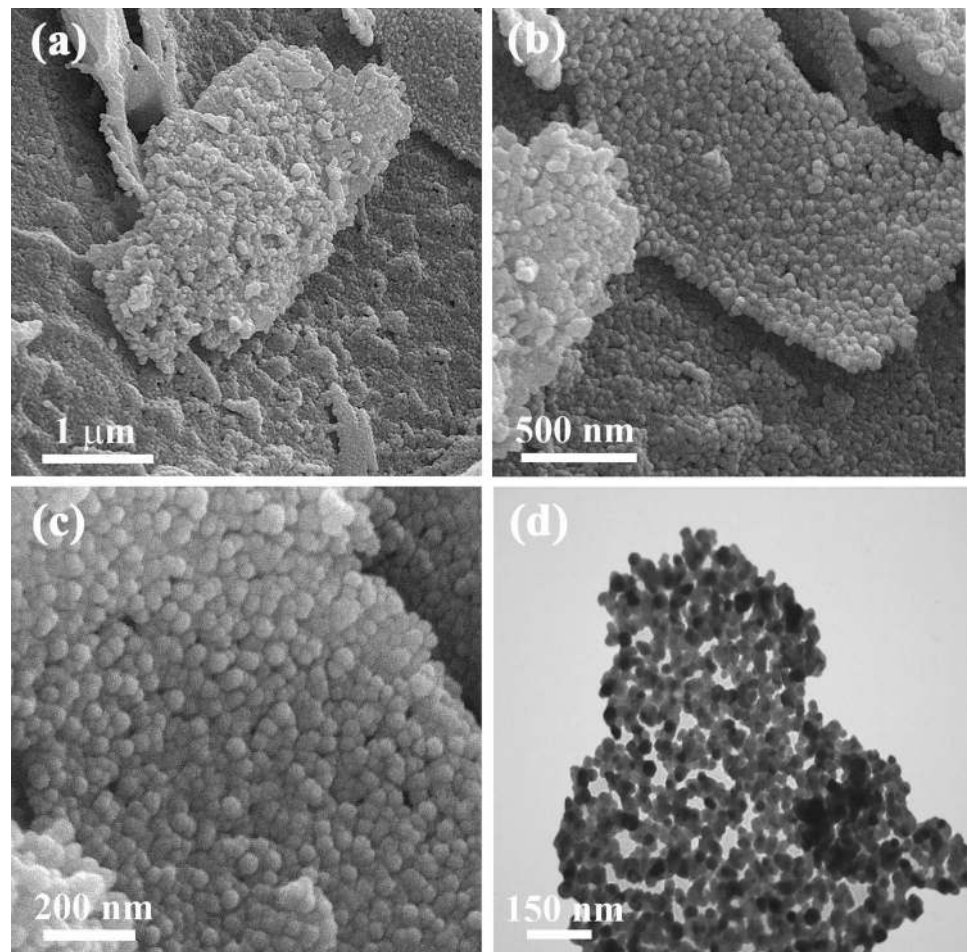


shown in Fig. 10d, some ZnO microspheres have hollow shaped nature. The hollow microstructures are constructed from nanorods extending through the shell of sphere along the radial direction. FESEM studies performed on ZnO samples treated at different hydrothermal temperatures suggest the average size of $\sim$ (30 nm $\pm$ 1 nm), $\sim$ (210 nm $\pm$ 1 nm) and $\sim$ (119 nm $\pm$ 1 nm) for S150, S200 and S250 samples, respectively. The obtained mean sizes exhibit a trend similar to mean crystalline sizes estimated from XRD patterns as given in the supporting information (Table S1).

## 4 Discussion

We attempt to deduce information about the effect of synthesis temperature on linear and nonlinear optical characteristics of hydrothermally grown ZnO samples. The PL analysis revealed an enhancement in the intensity of SW emission with increasing synthesis temperature during the hydrothermal growth process. This can be attributed to the higher crystallinity of ZnO nanostructures obtained at higher synthesis temperatures, as confirmed by XRD analysis (Fig. S1) and the dimensionless parameter $I_{LW}/I_{SW}$ (Table 1). In addition, better crystallinity leads to reduced absorption intensity in the samples prepared at higher growth temperatures (Fig. S1). Amorphous materials are known to absorb light due to transitions in the defects that are prevalent in such structures.

Kerr-type nonlinear optical performance of ZnO samples prepared at different hydrothermal temperatures can originate from two distinct possibilities. The emergence of higher third-order optical characteristics in samples S200 and S250 than those obtained for sample S150 implies the possible influence of crystalline structure on Kerr-type optical nonlinearities. Samples treated at higher hydrothermal temperatures exhibit larger nonlinearities, which may be attributed to crystalline quality improvement in which non-stoichiometry is reduced as the oxygen

**Fig. 9** FESEM images of ZnO sample prepared at hydrothermal temperature of 200 °C
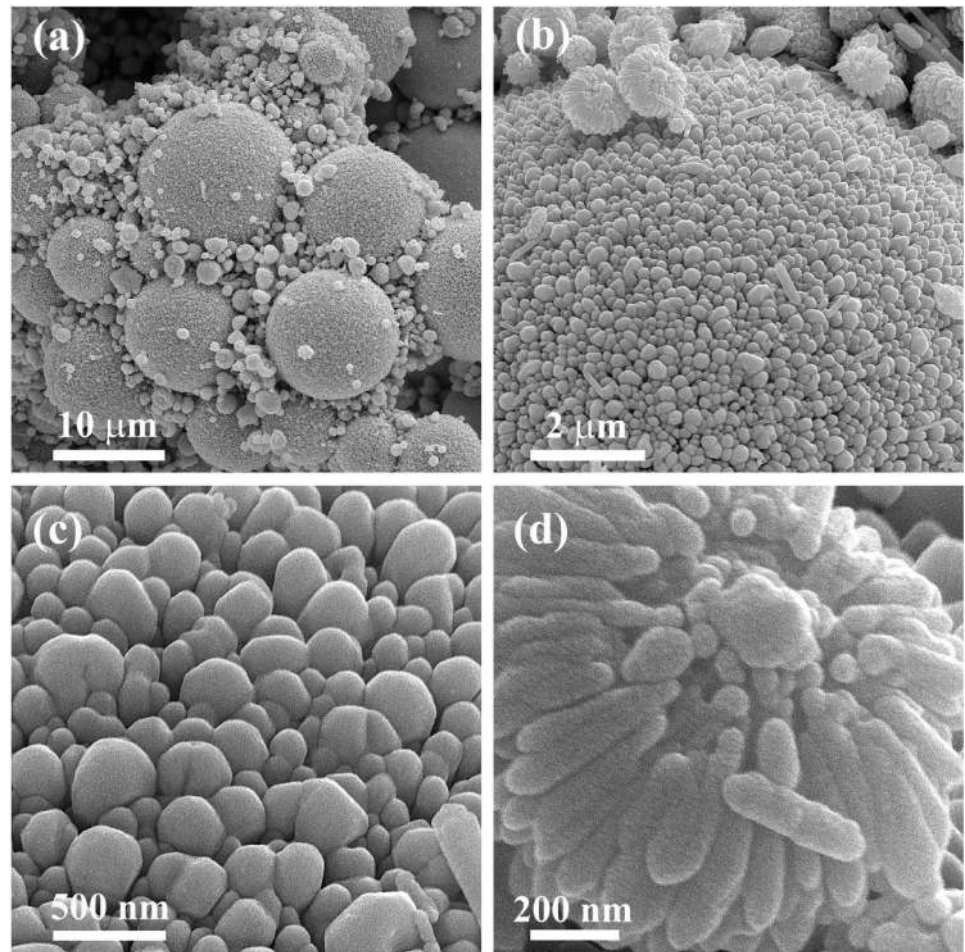


vacancies are filled with increasing growth temperature (Table 1). However, the highest Kerr-type optical parameters were found for sample S250, suggesting the synergistic effect of surface morphology on optical nonlinearities. The increased nonlinearities can be affected by increasing the photon-exposure sites originating from hollow porous microspheres of sample S250 compared to solid structures formed in samples S200 and S150. The obtained results confirm that controlling of hydrothermal temperature is essential for nonlinear optical performance. In addition, it needs to be emphasized that although the relatively low absorption of ZnO samples at 1064 nm can minimize the possibility of the contribution of thermal effects, the conversion of the absorbed energy into phonons from non-radiative absorption processes may not be negligible, when excitation occurs under high-repetition rate laser sources with the nano-second pulse width regime. Actually, the

Gaussian laser beams during their long-term interactions with ZnO samples can be partially adsorbed and then converted to heat to form a lens-like optical element due to cumulative thermal effects [72].

Indeed, it is rational to compare the obtained results with those found for structures reported in the literature for approximately similar experimental conditions. The comparative study reveals considerable differences in both magnitude and the sign of Kerr-type nonlinearities estimated in current work with those listed in Table 3. The Z-scan measurements indicate positive Kerr-type nonlinear indices in order of $10^{-11}$ W/m$^2$ for hydrothermally grown ZnO samples (Table 2), which are about 10 times higher than negative nonlinearities given in Table 3. It should be noted that although all the samples were illuminated by a similar laser system, there is a difference in the acquired radiation intensity. As it was noted, hydrothermally grown samples have been

**Fig. 10** FESEM images of ZnO sample prepared at hydrothermal temperature of 250 °C
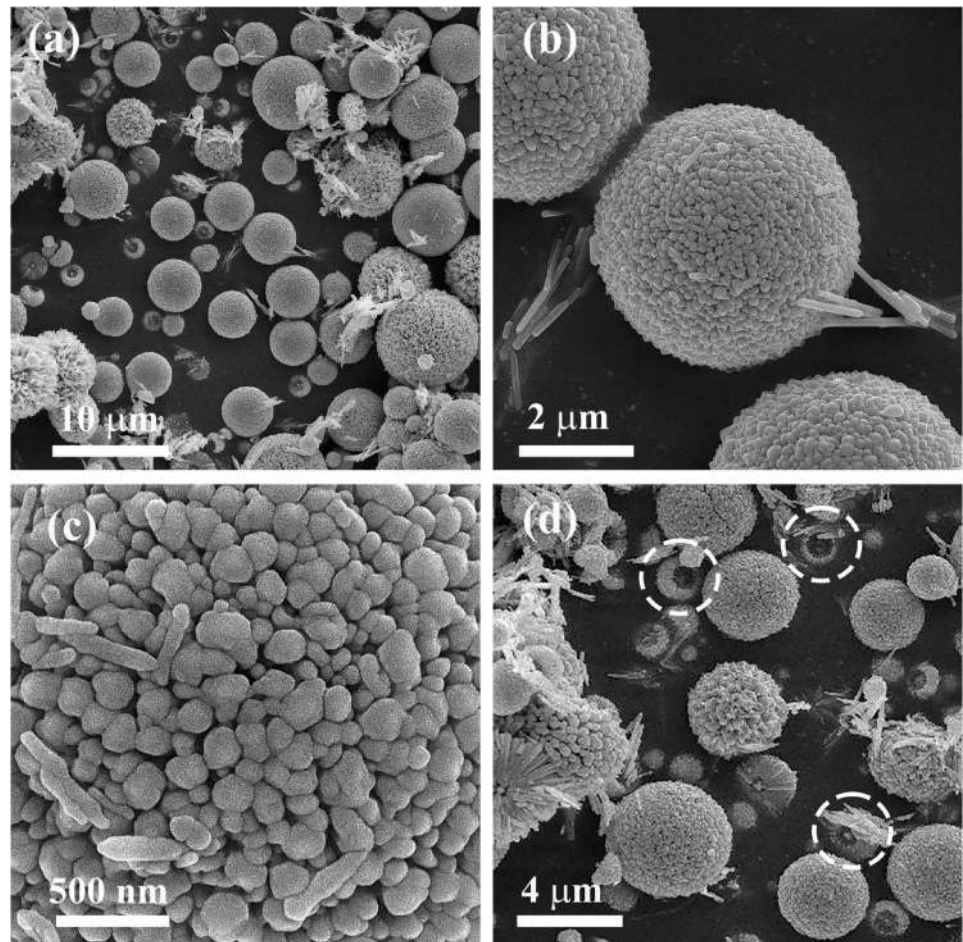


**Table 3** The nonlinear refractive index of different nanostructures (wavelength 1064 nm, pulse duration 50 ns, repetition rate 10 kHz, radiance power 63 mW, and laser intensity $1.25 \times 10^7$ W/$m^2$)

| Material | $n^2$ | Refs. |
|---|---|---|
| TiO$_2$ nanoparticles | $- 3.9 \times 10–12$ W/$m^2$ | [48] |
| TiO$_2$/ZnO core/shell nanoparticles | $- 3.84 \times 10–12$ W/$m^2$ | [48] |
| ZnS nanoparticles | $- 6.4 \times 10–12$ W/$m^2$ | [59] |
| ZnS/Ag$_2$S core/shell nanoparticles | $- 61.4 \times 10–12$ W/$m^2$ | [59] |
| ZnS/Ag$_2$S nanocomposites | $- 49.0 \times 10–12$ W/$m^2$ | [9] |
| CeO$_2$ nanoparticles | $- 3.5 \times 10–12$ W/$m^2$ | [19] |
| Ag/CeO$_2$ Schottky-type heterostructures | $- 49.7 \times 10–12$  W/$m^2$ | [19] |
| Ag-doped CeO$_2$ nanostructures | $- 11.5 \times 10–12$ W/$m^2$ | [20] |

exposed to laser beams with the intensity of $3.98 \times 10^6$ W/$m^2$, which is $\sim 10$ times lower than the irradiation intensity on the nanostructures presented in Table 3 ($1.25 \times 10^7$ W/$m^2$). The current data could also be comparable with that measured for erbium-doped zinc oxide thin films at wavelength of 1064 nm using the third harmonic generation (THG), showing a third-order nonlinear susceptibility of $\sim 10^3$ times higher than those estimated in the current study [73]. Many reports have been published focusing on nonlinearities of ZnO nanostructures. In Table 4, we have summarized examples of numerical values of nonlinear refractions measured using Z-scan technique of different ZnO structures.

**Table 4** The nonlinear refractive index of ZnO nanostructures

| Material | $(nm)\lambda$ | $n^2$ | Refs. |
|---|---|---|---|
| ZnO | 532 | $5.0 \times 10{-}17$ W/cm$^2$ | [74] |
| ZnO/Ag | 532 | $6.1 \times 10{-}17$ W/cm$^2$ | [74] |
| ZnO | 532 | $1.183 \times 10{-}13$ W/m$^2$ | [75] |
| ZnO/Graphene | 532 | $4.255 \times 10{-}13$ W/m$^2$ | [75] |
| ZnO/Al | 532 | $- 8.5 \times 10{-}12$ W/cm$^2$ | [76] |
| ZnO/Al | 1064 | $- 1.25 \times 10{-}11$ W/cm$^2$ | [76] |
| ZnO | 532 | $5.9 \times 10{-}15$ W/m$^2$ | [76] |
| ZnO | 532 | $1.5 \times 10{-}17$ W/m$^2$ | [77] |
| ZnO/Ag | 532 | $11.3 \times 10{-}17$ W/m$^2$ | [78] |
| ZnO/Sr | 532 | $7.96 \times 10{-}12$ W/cm$^2$ | [79] |

## 5 Conclusions

In summary, a simple hydrothermal procedure using zinc acetate dihydrate/glycerol aqueous solution was successfully utilized to fabricate hollow ZnO microspheres self-assembled by rod-like nanostructures. The morphology of ZnO microspheres could be adjusted by changing the hydrothermal treatment temperatures (150, 200, and 250 °C) during reaction process. A plausible formation mechanism was suggested to describe self-assembly of rod-like ZnO nanostructures into hollow microspheres. Morphology-dependent linear optical characteristics were justified using photoluminescence and UV–Vis absorbance spectra, showing red-shifts and improved crystalline qualities with increasing hydrothermal growth temperature. Kerr-type optical nonlinearities were studied using the Z-scan method under a pulsed laser system operating at 1064 nm. The Z-scan analysis exhibited the positive lens effect presenting self-focusing behavior in all the tested samples. The highest Kerr-type optical susceptibility was found to be $2.31 \times 10^{-6}$ esu for the sample treated at a hydrothermal temperature of 250 °C. The obtained results reveal the synergistic effect of surface morphologies to provide promising routes for developing nonlinear optical materials in future technologies.

## Author contributions

A.H. designed and conceived the idea. M. O prepared the samples. A.H. developed the project, analyzed data and interpreted the results. A.H. and J.D. jointly wrote and developed the manuscript. B.M. contributed in designing of the experiments and discussions. M.S. and J.D. contributed in interpretation of the obtained results and discussions, checking, and revising the manuscript.

## Declarations

**Conflict of interest** The authors declare no competing interests.

**Consent to participate** Consent was obtained from all authors prior to, during and now for submission.

**Consent to publication** All the authors agree to publication of the manuscript in its current form.

**Supplementary Information:** The online version contains supplementary material available at http s://doi.org/10.1007/s10854-021-06827-0.

# References

1. J. Kerr, X.L. Mag, J. Sci. **50**, 337 (1875)
2. M. Sheik-Bahae, J. Wang, E.W. Van Stryland, IEEE J. Quantum Electron **30**, 249 (1994)
3. H.R. Hamedi, Phys. B **442**, 60 (2014)
4. Y. Wu, X. Yang, Appl. Phys. Lett **91**, 94104 (2007)
5. Y. Wu, Phys. Rev. A **54**, 1586 (1996)
6. S.H. Asadpour, H.R. Hamedi, M. Sahrai, J. Lumin. **132**, 2188 (2012)
7. W. Jiang, J. Song, H. Zheng, C. Wu, B. Yin, Y. Zhang, Opt. Commun. **282**, 101 (2009)
8. P.R. Hemmer, D.P. Katz, J. Donoghue, M. Cronin-Golomb, M.S. Shahriar, P. Kumar, Opt. Lett. **20**, 982 (1995)
9. M. Kiani, A. Haghighatzadeh, J. Inorg. Organomet. Polym. Mater **31**, 229 (2020)
10. X.-Y. Yan, K.-X. Zhang, C.-B. Yao, Q.-H. Li, Mater. Lett **176**, 49 (2016)
11. S. Thakur, B. Semnani, S. Safavi-Naeini, A.H. Majedi, Sci. Rep **9**, 1 (2019)
12. H. Qian, Y. Xiao, Z. Liu, Nat. Commun. **7**, 13153 (2016)
13. H. Li, F. Zhou, X. Zhang, W. Ji, Appl. Phys. B **64**, 659 (1997)
14. H. Wang, D. Goorskey, M. Xiao, Phys. Rev. Lett **87**, 73601 (2001)
15. X.C. Jiang, Y.W. Zhou, D.L. Gao, Y. Huang, L. Gao, Opt. Express **28**, 17384 (2020)
16. H. Zhou, D. Gao, L. Gao, Plasmonics **13**, 623 (2018)
17. Z. Dehghani, S. Nazerdeylami, E. Saievar-Iranizad, M.H.M. Ara, J. Phys. Chem. Solids **72**, 1008 (2011)
18. R. Merikhi, B. Bennecer, A. Hamidani, J. Magn. Magn. Mater **424**, 327 (2017)
19. A. Haghighatzadeh, B. Mazinani, Opt. Laser Technol **131**, 106426 (2020)
20. A. Haghighatzadeh, Opt. Laser Technol **126**, 106114 (2020)
21. A. Haghighatzadeh, M. Hosseini, B. Mazinani, M. Shokouhimehr, Mater. Res. Express **6**, 115060 (2019)
22. R. Yan, D. Gargas, P. Yang, Nat. Photonics **3**, 569 (2009)
23. Ü. Özgür, Y.I. Alivov, C. Liu, A. Teke, M. Reshchikov, S. Doan, V. Avrutin, S.-J. Cho, H. Morkoç, J. Appl. Phys **98**, 11 (2005)
24. D. Panda, T.-Y. Tseng, J. Mater. Sci **48**, 6849 (2013)
25. S. Dhara, P.K. Giri, Rev. Nanosci. Nanotechnol **2**, 147 (2013)
26. S. Baruah, J. Dutta, Sci. Technol. Adv. Mater **10**(1), 013001 (2009)
27. S.Y. Bae, H.W. Seo, J. Park, J. Phys. Chem. B **108**, 5206 (2004)
28. P.-C. Chang, Z. Fan, D. Wang, W.-Y. Tseng, W.-A. Chiou, J. Hong, J.G. Lu, Chem. Mater **16**, 5133 (2004)
29. X.P. Gao, Z.F. Zheng, H.Y. Zhu, G.L. Pan, J.L. Bao, F. Wu, D.Y. Song, Chem. Commun. **12**, 1428 (2004)
30. C.-L. Kuo, T.-J. Kuo, M.H. Huang, J. Phys. Chem. B **109**, 20115 (2005)
31. B. Cheng, E.T. Samulski, Chem. Commun. **8**, 986 (2004)
32. M.S. Tokumoto, S.H. Pulcinelli, C.V. Santilli, V. Briois, J. Phys. Chem. B **107**, 568 (2003)
33. T.S. Tofa, K.L. Kunjali, S. Paul, J. Dutta, Environ. Chem. Lett **17**, 1341 (2019)
34. H.R.B.A. Rahim, M.Q.B. Lokman, S.W. Harun, J. Dutta, W.S. Mohammed, Sens. Actuators A **257**, 15 (2017)
35. J. Burgin, M. Liu, P. Guyot-Sionnest, J. Phys. Chem. C **112**, 19279 (2008)
36. Q. Xu, I. Tonks, M.J. Fuerstman, J.C. Love, G.M. Whitesides, Nano Lett **4**, 2509 (2004)
37. C.L. Nehl, H. Liao, J.H. Hafner, Nano Lett **6**, 683 (2006)
38. P.R. Sajanlal, T.S. Sreeprasad, A.S. Nair, T. Pradeep, Langmuir **24**, 4607 (2008)
39. S. Baruah, J. Dutta, J. Cryst. Growth **311**, 2549 (2009)
40. H. Guo, X.-Y. Lu, Y. Pei, H. Chua, B. Wang, K. Wang, Y. Yang, Y. Liu, RSC Adv. **4**, 37431 (2014)
41. L. Zhou, Z. Han, G.-D. Li, Z. Zhao, J. Phys. Chem. Solids **148**, 109719 (2021)
42. S. Haghighi, A. Haghighatzadeh, Appl. Phys. A **126**(2), 1 (2020)
43. T. Jiang, Y. Wang, D. Meng, X. Wu, J. Wang, J. Chen, Appl. Surf. Sci **311**, 602 (2014)
44. Y. Wang, T. Jiang, D. Meng, J. Yang, Y. Li, Q. Ma, J. Han, Appl. Surf. Sci **317**, 414 (2014)
45. Q. Chen, Y. Wang, M. Zheng, H. Fang, X. Meng, J. Mater. Sci. Mater. Electron **29**, 19757 (2018)
46. E. Alp, E.C. Araz, A.F. Buluç, Y. Murgüner, Y. Deer, H. Egin, K.B. Dermenci, M.K. Kazmanl, S. Turan, A. Genç, Adv. Powder Technol **29**, 3455 (2018)
47. M.A. Lamrani, M. Addou, Z. Sofiani, B. Sahraoui, J. Ebothe, A. El Hichou, N. Fellahi, J.C. Bernede, R. Dounia, Opt. Commun. **277**, 196 (2007)
48. A. Haghighatzadeh, B. Mazinani, Appl. Phys. B **126**, 1 (2020)
49. M. Hosseini, A. Haghighatzadeh, B. Mazinani, Opt. Mater. (Amst) **92**, 1 (2019)
50. P. Loiko, T. Bora, J.M. Serres, H. Yu, M. Aguiló, F. Díaz, U. Griebner, V. Petrov, X. Mateos, J. Dutta, Beilstein J. Nanotechnol. **9**, 2730 (2018)
51. A. Zawadzka, P. Póciennik, J. Strzelecki, B. Sahraoui, Opt. Mater. **37**, 327 (2014)

52. J. Livage, Materials (Basel) **3**, 4175 (2010)

53. M. Zhou, X. Zhang, J. Wei, S. Zhao, L. Wang, B. Feng, J. Phys. Chem. C **115**, 1398 (2010)

54. J. Thomas, P. Periakaruppan, V. Thomas, J. John, S. Mathew, T. Thomas, J. Jose, I. Rejeena, A. Mujeeb, RSC Adv. **8**, 41288 (2018)

55. H. Maki, R. Chiba, T. Onodera, H. Kasai, R. Sato, Y. Takeda, H. Oikawa, MRS Commun. **9**, 1087 (2019)

56. H. Oikawa, Bull. Chem. Soc. Jpn. **84**, 233 (2011)

57. Y. Li, D.-L. Li, J.-C. Liu, Chinese Chem. Lett. **26**, 304 (2015)

58. X. Chen, A. Wang, M. Yin, L. Cheng, J. Zhang, C. Li, W. Zhu, D. Shang, Dye. Pigment **167**, 189 (2019)

59. A. Haghighatzadeh, M. Kiani, B. Mazinani, J. Dutta, J. Mater. Sci. Mater. Electron. **31**, 1283 (2020)

60. Q.L. Ma, R. Xiong, B. Zhai, Y.M. Huang, Appl. Surf. Sci. **324**, 842 (2015)

61. U. Vinoditha, B.K. Sarojini, K.M. Sandeep, B. Narayana, S.R. Maidur, P.S. Patil, K.M. Balakrishna, Appl. Phys. A **125**, 436 (2019)

62. S. Kuriakose, B. Satpati, S. Mohapatra, Phys. Chem. Chem. Phys **16**, 12741 (2014)

63. P.-T. Hsieh, Y.-C. Chen, K.-S. Kao, C.-M. Wang, Appl. Phys. A **90**, 317 (2008)

64. S. Agarwal, P. Rai, E.N. Gatell, E. Llobet, F. Güell, M. Kumar, K. Awasthi, Sens. Actuators B **292**, 24 (2019)

65. R. Del Coso, J. Solis, JOSA B **21**, 640 (2004)

66. V. Dimitrov, S. Sakka, J. Appl. Phys **79**, 1741 (1996)

67. M.D. Zidan, M. Al-Ktaifani, A. Allahham, Opt. Laser Technol. **70**, 45 (2015)

68. M.R. Sharifimehr, K. Ayoubi, E. Mohajerani, Opt. Mater. (Amst) **49**, 147 (2015)

69. J.L.J. Pérez, R. Gutiérrez-Fuentes, J.F.S. Ramírez, O.U.G. Vidal, D.E. Téllez-Sánchez, Z.N.C. Pacheco, A.C. Orea, J.A.F. García, Adv. Nanopart. **2**, 223 (2013)

70. W. Balogun, Y.K. Sanusi, A.O. Aina, Int. J. Dev. Res **8**(01), 18486 (2018)

71. B. Al-Nashy, S.M.M. Ameen, A.H. Al-Khursan, Results Phys **6**, 189 (2016)

72. N. Karampitsos, D. Kyrginas, S. Couris, Opt. Lett **45**, 1814 (2020)

73. M.A. Lamrani, M. El Jouad, M. Addou, T. El Habbani, N. Fellahi, K. Bahedi, M.E. Touhami, Z. Essaïdi, Z. Sofiani, B. Sahraoui, Spectrosc. Lett **41**, 292 (2008)

74. A. S. Rao, G. Sethuraman, O.S.N. Ghosh, A. Sharan, A. K. Viswanath, ArXiv 1806, 09404 (2018)

75. E. Solati, D. Dorranian, Appl. Phys. B **122**, 76 (2016)

76. J.H. Castro-Chacón, C. Torres-Torres, A.V. Khomenko, M.A. García-Zárate, M. Trejo-Valdez, H. Martínez-Gutiérrez, R. Torres-Martínez, J. Mod. Opt **64**, 601 (2017)

77. L. Irimpan, B. Krishnan, V.P.N. Nampoori, P. Radhakrishnan, J. Colloid Interface Sci **324**, 99 (2008)

78. K.-X. Zhang, C.-B. Yao, X. Wen, Q.-H. Li, W.-J. Sun, RSC Adv. **8**, 26133 (2018)

79. K.M. Rahulan, T. Sahoo, N.A.L. Flower, I.P. Kokila, G. Vinitha, R.A. Sujatha, Opt. Laser Technol. **109**, 313 (2019)